LANGMUIR

pubs.acs.org/Langmuir Article

Natural Cellulose Fiber-Derived Photothermal Aerogel for Efficient and Sustainable Solar Desalination

Hoang Giang Nguyen, Thi An Hang Nguyen, Danh Bich Do, Xuan Nui Pham, Tuan Hong Nguyen, Ha Lien Thi Nghiem, Minh Viet Nguyen, and Tien Thanh Pham*

Cite This: *Langmuir* 2023, 39, 6780–6793 Read Online

ACCESS | Metrics & More | Article Recommendations | Supporting Information

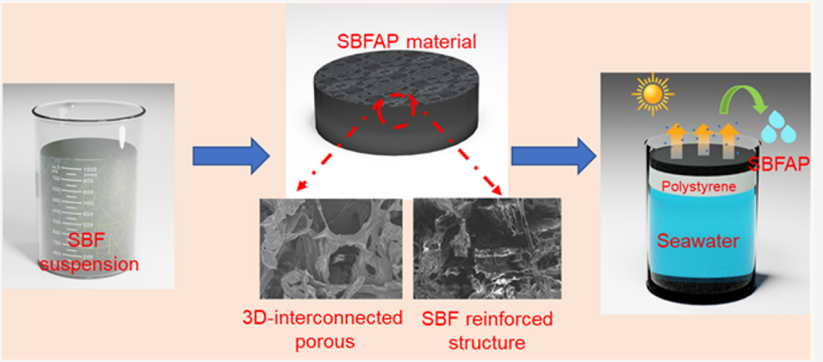

ABSTRACT: Aerogels are becoming a promising platform to fabricate photothermal materials for use in solar steam generation (SSG), which have remarkable application potential in solar desalination, due to their excellent thermal management, salt resistance, and considerable water evaporation rate. In this work, a novel photothermal material is fabricated by forming a suspension between sugarcane bagasse fibers (SBF) and poly(vinyl alcohol), tannic acid (TA), and Fe^{3+} solutions via hydrogen bonds of hydroxyl groups. After freeze drying, the fabricated SBF aerogel-based photothermal (SBFAP) material possesses a 3D interconnected porous microstructure, which could enhance water transportation ability, reduce thermal conductivity, and quickly dissolve salt crystals on the SBFAP surface. Thanks to the formation of micro/nanosized complexes between TA and Fe^{3+} ions on the SBFAP material, the SBFAP exhibits high light capture and water evaporation rate (2.28 kg m^{-2} h^{-1}). In particular, due to strong hydrogen bonding and the SBF, the SBFAP material is reinforced, thereby exhibiting excellent structural stability in seawater. Moreover, the high salt tolerance of SBFAP favors its high desalination performance for at least 76 days of continuous evaporation under actual conditions. This research paves the way for the fabrication of natural cellulose fiber-based photothermal materials for application in solar desalination.

INTRODUCTION

Approximately 75 percent of the Earth's surface is covered in water. Over 97 percent of this water is found in oceans as salt water (seawater). Clearly, seawater is an infinite natural resource that sustains the development of human beings. For instance, a large amount of salt for human consumption is produced from seawater.[1] Precious metals such as uranium and lithium,[2,3] used in nuclear energy and lithium-ion batteries, are also extracted from seawater. Notably, due to the development of desalination technologies, seawater has become a vital resource for producing fresh water to ensure sustainable development, given the water scarcity caused by environmental pollution, water resource depletion, and climate change.[4,5] In recent years, solar steam generation (SSG) systems, which are applied in seawater desalination to produce freshwater, have attracted great interest of scientists worldwide because of their simple installation, easy operation, and renewable energy consumption.[4,6−8] Besides, with a capacity of approximately 10.95 kg m^{-2} d^{-1}, the SSG-based seawater desalination can be considered a low-cost solution for producing freshwater at the household scale.[7] The SSG systems harness solar energy and transfer it into thermal energy to evaporate water into steam at the water−air interface of a photothermal material.[9−11] Therefore, the thermal management in photothermal materials, which is associated with photothermal conversion ability, minimizing heat loss, harnessing thermal energy from the environment, bulk water, and thermal radiation, plays a crucial role in improving the SSG system's performance.[6,11,12] Also, it

Received: February 1, 2023
Revised: April 20, 2023
Published: May 4, 2023

https://doi.org/10.1021/acs.langmuir.3c00297
Langmuir 2023, 39, 6780−6793

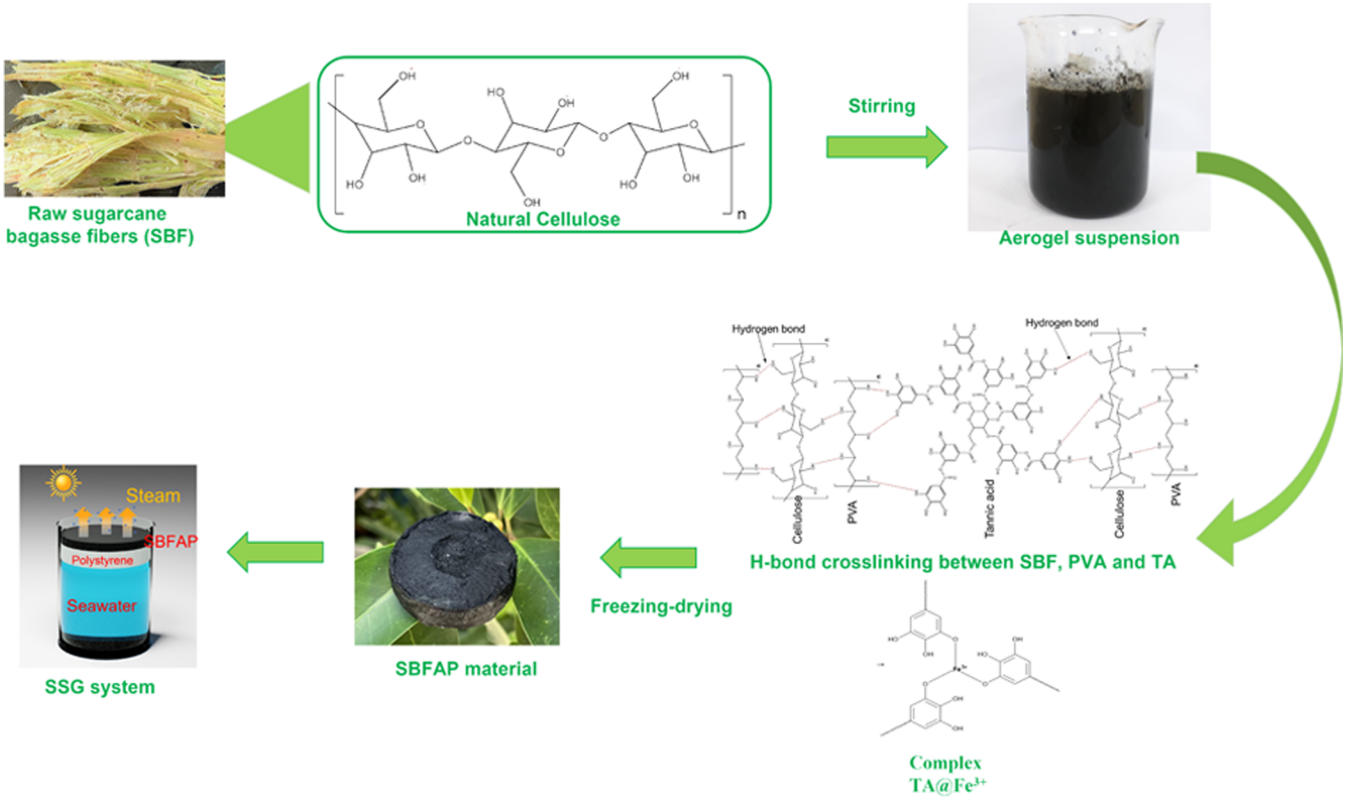

Figure 1. Schematic of the SBFAP material-based SSG system.

is recently reported that reducing the enthalpy of water evaporation is vital in enhancing the water evaporation rate of a photothermal material.[7,13] Besides, other aspects of photothermal materials when applied in seawater desalination (e.g., structural stability, self-cleaning ability, etc.) are investigated to improve their long-term performance and actual application.[14−16] Hence, seeking substrate materials with superior properties has become the main goal in recent studies on photothermal materials. Substrates, such as metallic nanoparticles,[17] semiconductors,[18] polymers,[10] carbon-based materials,[19] and biomass, have been widely used for the fabrication of photothermal materials with various morphologies (e.g., 2D, 3D interconnected porous, hierarchical, conical structures, etc.).[19,20] Consequently, the water evaporation performance of the SSG could reach approximately 2−4 kg m^{-2} h^{-1}, with an energy utilization efficiency of 100% for a relatively 3D-structural photothermal material.[13,21] However, the practical application of 3D-structural photothermal materials is still restricted due to their high fabrication cost and low structural stability during preservation and transportation.[22−24] Thus, future work is still needed to address these challenges.

Recently, aerogels, as potential substrate materials for the preparation of photothermal materials, have attracted much attention.[24−26] This is because aerogels possess many favorable properties, namely (1) 3D interconnected porous structure with a large specific surface area that increases the water transportation ability,[14] (2) high porosity and low density that reduce the thermal conductivity,[27] (3) simple fabrication method, in which freeze drying is a significant step,[28,29] and (4) numerous hydroxyl groups that help reduce the enthalpy of water evaporation.[30,31] The aerogels used to fabricate photothermal materials were first proposed by combining a bacterial cellulose biomaterial with a graphene oxide layer.[32] Till date, various aerogels have been used as substrates for photothermal material production. For example, (1) aerogels derived from polymers, such as polypyrrole/poly (vinyl alcohol) (PPy/PVA),[13,29] poly(3,4-ethylenedioxythiophene):polystyrene sulfonate/nanofibrillated cellulose (PEDOT:PSS/NFC), etc.,[14] (2) aerogels originating from inorganic materials such as silica (SiO_2),[33] graphene oxide (GO),[23] carbon nanotubes (CNTs),[34] etc., and (3) aerogels produced from natural cellulose fibers (e.g., waste cotton fabrics, corn straw, etc.).[14,28]

To fabricate the aerogel-based photothermal materials with high sunlight absorption ability, diversified methods have been utilized, such as dispersing active carbon or CNTs in a polymer suspension,[33,35] production of a bilayer structure between MoS_2 and the aerogel,[21] formation of crosslinks with polymers that have high light absorption ability such as PPy, PEDOT:PSS,[14] and polydopamine (PDA).[36] Besides, the multilayer and 3D interconnected porous structures and the microsized capillary structure of aerogels have been found to improve their light trapping ability. In addition, the aerogel-based photothermal material has low thermal conductivity (0.03−0.1 W m^{-1} K^{-1}), low density (0.06 g/cm^3), and high porosity (>90%).[30,33,36] Therefore, the photothermal material acts as an insulator foam in the SSG, limiting the heat energy loss to the environment. Since the aerogels were formed by crosslinks of hydrogens, photothermal materials with 3D structures can be easily fabricated. Therefore, the increase in the side area of photothermal materials plays an essential role in improving the SSG's performance. Besides, the aerogel-based photothermal materials demonstrate an excellent self-cleaning property. Consequently, salt crystals, deposited on the material surface during seawater desalination, can be quickly dissolved.[24,25] Nevertheless, since the crosslinking of hydrogens or Si-O-C forms aerogels, the structural stability in

https://doi.org/10.1021/acs.langmuir.3c00297
Langmuir 2023, 39, 6780−6793

Table 1. Concentrations, Ratios of Ingredients, and Ultimate Tensile Strengths of the Fabricated Materials

sample	SBF (g/100 mL)	PVA (g/100 mL)	TA (g/100 mL)	$FeCl_3·6H_2O$ (g/100 mL)	ultimate tensile strength (kPa)
SBF aerogel	2.0	4.0			53.0
SBFAP (1:2)	2.0	4.0	0.3	0.6	64.0
SBFAP (1:1)	2.0	4.0	0.6	0.6	72.0

seawater usually is poor, limiting the practical application.[29,33] Besides, to improve the light absorption ability of photothermal materials, costly materials (e.g., PPy, PDA, PEDOT:PSS, CNT, etc.) were used, leading to an increased fabrication cost.[29,34] Therefore, it is crucial to fabricate an aerogel-based photothermal material with excellent structural stability and efficient water evaporation using a simple and low-cost procedure.[37]

The biomass materials and natural celluloses, extracted from waste cotton fabrics, were utilized in the fabrication of photothermal materials in an attempt to reduce their fabrication costs while enhancing their structural stability.[24,38,39] The agar hydrogel (AHG), which was derived from natural algae, was used to prepare a photothermal material by immobilizing Prussian blue nanoparticles on a cellulose nanofiber (CNF-PB).[38] With the salt rejection ability of the AHG, the photothermal material exhibited a stable performance under long-term seawater desalination. Moreover, the agar powder was also combined with TiN nanoparticles to increase the water evaporation rate and the lifespan of the fabricated photothermal material.[39] A fully biomass-based photothermal material was fabricated by forming a hydrogel layer between the cellulose−lignin composite and lignin-derived carbon.[40] The lignin present in the hydrogen could improve the water transport rate and the durability of the fabricated photothermal material. As a result, the aerogel photothermal material based on a biomass material (natural cellulose fibers) demonstrated a high water evaporation rate and durability in seawater conditions. This was attributed to the numerous OH^- groups in the biomass that could easily form strong hydrogen bonds with substrate polymers. This indicates that the hydrogen crosslinking in aerogels and hydrogels plays a vital role in improving the structural stability of a photothermal material. Therefore, using polyphenols for the preparation of aerogels is expected to intensify the strength of the resultant materials.

In order to do that, tannic acid (TA), a low-cost and eco-friendly chemical, was used as a ligand bridge to form complexes with metallic nanoparticles.[41] It is expected to enhance the light absorption ability of the photothermal material used in the SSG. Since TA consists of numerous OH groups attached to the aromatic rings, the link between TA and the substrate material via hydrogen bonds is quite stable, thereby enhancing the structural stability of the absorber layer in the photothermal material under various conditions.[41] This study aims at turning the natural cellulose fiber, which is derived from the waste sugarcane bagasse (SB), into the photothermal material with high performance in the SSG system (Figure 1).[42] The photothermal material was fabricated by forming a suspension between the sugarcane bagasse fiber (SBF) and poly(vinyl alcohol) (PVA), TA, and Fe (III) solutions via the hydrogen bonds of hydroxyl groups. After freeze drying, the fabricated SBF aerogel-based photothermal (SBFAP) material possessed a 3D interconnected porous microstructure, which could enhance water transportation ability, reduce thermal conductivity, and quickly dissolve salt crystals on the SBFAP surface. In particular, the SBFAP material was reinforced due to strong hydrogen bonds among SBF, PVA, and TA, thus exhibiting excellent structural stability in seawater. Then, with its high salt tolerance, the SBFAP material could maintain high desalination performance for at least 76 days of continuous evaporation under real conditions. The desalination device, which was designed with the fabricated photothermal material, exhibited a high efficiency in seawater desalination and excellent structural stability and thus could be used in the practical application.

EXPERIMENTAL SECTION

Materials. Ethanol absolute (99.7%), sodium hydroxide (NaOH, 96%), and iron (III) chloride hexahydrate ($FeCl_3·6H_2O$, 99%) were provided by GHTECH (China). Poly(vinyl alcohol) (PVA-124, 97%) and sodium hypochlorite (NaClO, 8%) were purchased from Xilong Scientific (China). All chemicals used for the experiments in this work were analytical grade. Sugarcane-based cellulose fibers were fabricated from sugarcane bagasse collected from sugarcane juice stores in Hanoi, Vietnam. The procedure for SBF fabrication is described in Figure S1 of the Supporting Information. The seawater for desalination tests was collected from Vietnam's East Sea (Quang Ninh, Vietnam).

Fabrication of the Photothermal Material. The procedure for the SBF aerogel is described in Figure S2 of the Supporting Information. The SBF aerogel-based photothermal material was fabricated as follows: First, 0.3−1 g of TA and 2 g of SBF were mixed with 100 mL of DI water for 30 min at 28 ± 1 °C to obtain the TA@SBF solution. The concentrations of TA and SBF in the solution are shown in Table 1. In the next step, 0.6 g of $FeCl_3·6H_2O$ and 4 g of PVA were dissolved in 100 mL of DI water for 1 h at 28 ± 1 °C to obtain the PVA@Fe solution. Then, 100 mL of the TA@SBF solution and 100 mL of the PVA@Fe solution were mixed together. After that, the mixture was ultrasonicated at 200 W for 10 min to form the crosslinking between the -OH groups of the SBF, PVA, TA, and TA@Fe^{3+} complexes. The obtained suspension was cured at 80 °C for 3 h to accelerate the chemical reaction to form the crosslinker. Subsequently, it was frozen at −80 °C for 24 h in a refrigerator. Finally, the frozen sample was freeze-dried in a vacuum freeze dryer at −80 °C for 36 h to form aerogels. The obtained aerogels were labeled as shown in Table 1.

Photothermal Material Characterization. The morphologies of the fabricated SBF and SBFAP materials were investigated by scanning electron microscopy (SEM; Regulus 8100, Hitachi, Japan). An energy dispersive spectrometer (EDS; JED-2300, JEOL Ltd., Japan) was used for elemental analyses of both SBF and SBFAP samples. A Fourier transform infrared spectrometer (FTIR; FTIR-4600, JASCO, Japan) was employed to examine the functional groups on the materials' surface. The crystal structures of the samples were explored using an X-ray diffractometer (XRD; Mini Flex 600, Rigaku, Japan). The enthalpy values of water evaporation at different conditions were determined using differential scanning calorimetry (DSC, Rigaku, Japan). The reflection (R) and transmission (T) spectra of the SBF aerogel samples were recorded using a UV−VIS−NIR spectrometer (Jasco V-770, Jasco, Japan). The light absorption capacities of aerogel samples were calculated from the obtained reflection and transmission. The hydrophilicity and wettability of the fabricated photothermal material were quantified with an optical contact angle meter. A THB-500 linseis (Germany) was utilized to measure the thermal conductivity of the SBFAP material based on the transient hot bridge principle. A thermal imaging camera (FLIR C2;

https://doi.org/10.1021/acs.langmuir.3c00297
Langmuir 2023, 39, 6780−6793

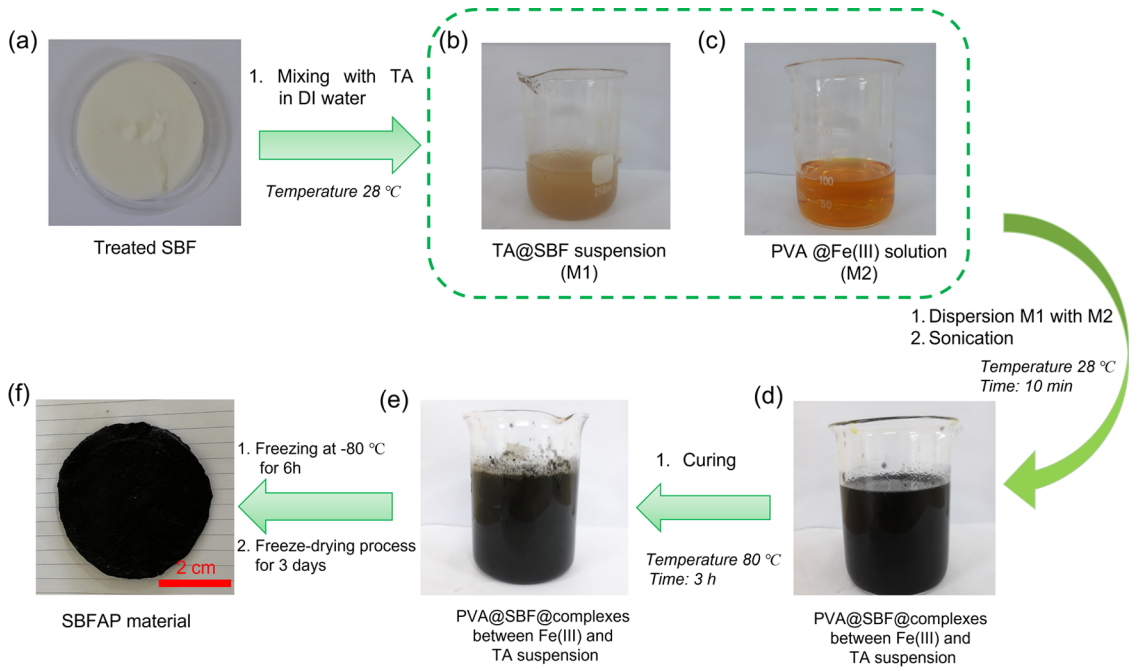

Figure 2. Fabrication of the SBFAP material using the polymerization crosslinking method. (a) Treated sugarcane bagasse fibers (SBF), (b) TA@SBF suspension, which was made by dissolving 0.6 g of TA and 2 g of SBF into 100 mL of DI water, (c) PVA@Fe(III) suspension, which was fabricated by dissolving 0.6 g of $FeCl_3 \cdot 6H_2O$ and 4 g of PVA in 100 mL of DI water, (d) PVA@SBF@complexes between Fe(III) and TA suspension made by mixing the TA@SBF suspension with the PVA@Fe(III) suspension, (e) PVA@SBF@complexes between Fe(III) and TA suspension after curing for 3 h, and (f) SBF aerogel-based photothermal (SBFAP) material.

FLIR Systems, Inc.) was used to measure the surface temperatures of the samples in thermal conversion and evaporation performances.

Solar Steam Evaporation Performances. The SSG system in Figure 1 was used to investigate the seawater evaporation performance of the SBFAP material. The polystyrene foam (thickness of 15−20 mm) was used as a thermal insulation layer, and cotton gauze (mesh size of 2 mm × 2 mm; Tanaphar, Vietnam) was wrapped around the polystyrene foam as a water transportation path. The SBFAP material was placed on this arrangement, and then, the structure was placed in a beaker. An optical power meter (Newport Corporation) was used to identify the power density of the solar simulator. The water evaporation experiments under indoor conditions were conducted using a solar simulator (Newport Corporation) with an AM 1.5G filter. The room temperature and air humidity were 28−30 °C and 40−70%, respectively. The change in the real-time water mass during the evaporation was monitored using an electronic balance (Mettler Toledo MS12002TS, Switzerland). The changes in temperature during the water evaporation were observed with an IR camera (FLIR C2). The ion concentrations in water were determined using a Due AAS 280FS/280Z (Agilent) and Spectro UV−VIS double spectrophotometer (UVD-3200, Labomed).

RESULTS AND DISCUSSION

Fabrication of the Photothermal Material. Raw sugarcane bagasse, which is a popular, cheap, abundantly available biomass in Vietnam, was used to prepare an aerogel for the fabrication of the photothermal material. In the first step (Figure S1), the raw sugarcane bagasse was treated with ethanol and NaOH to remove lignin and hemicellulose, respectively.[43,44] Next, it was plunged in NaOH/NaClO solution so that primary hydroxyl groups on the cellulose molecule could be oxidized to form oxidized microcrystalline cellulose.[26,43] The purification process caused an increase in the crystallinity index of the SBF, which was calculated in the next session. Then, the treated SBF (Figure 2a) was dispersed in the TA solution and in DI water to create H-bonds between -OH groups of the TA and the cellulose in the treated SBF, forming a suspension (TA@SBF suspension (Figure 2b)). The formation of H-bonds between the TA and SBF plays a crucial role in forming the light absorption layer as well as improving the mechanical stability of the fabricated SBFAP material.[36] After that, PVA and $FeCl_3 \cdot 6H_2O$ were completely dissolved in DI water and the PVA@Fe(III) solution was obtained (Figure 2c). In this process, the Fe^{3+} ions did not form complexes with the -OH groups of PVA. This can be explained by the difference between -OH groups of TA and those of the cellulose. While the former directly bonded to aromatic rings, the latter exhibited low polarity resulting from the absence of a conjugated system.[20] The TA@SBF solution was dispersed into 100 mL of PVA@Fe(III) solution; then, the mixture was ultrasonicated. The process formed crosslinking in the aerogel structure between the -OH groups of the SBF, PVA, TA (Figure S3a,b), and TA@Fe^{3+} complexes (Figure S3c).[41,43] In the suspension, PVA plays the role of a bridge to form cross-hydrogen bonds between the PVA, TA, and SBF (PVA@TA@SBF). Moreover, the -OH groups of the TA could form complex crosslinking with both CFB and PVA, thereby increasing the mechanical property of the obtained aerogel. In addition, the TA@Fe^{3+} complexes were formed on the crosslinking of the PVA@TA@SBF, and then, a homogeneous black suspension (Figure 2d) was obtained after the sonication. The high density of the TA@Fe^{3+} complexes was responsible for the black color of the suspension. The obtained suspension was cured at 80 °C for 3h to accelerate the chemical reaction to form the crosslinker (Figure 2e). After freeze drying, the SFB aerogel (Figure S4a) and SFB aerogel-based photothermal material (Figures 2f and S4b) were attained with different ratios of TA as shown in Table 1. Besides, when the concentration of TA reached 10 mg/mL, an aggregation (Figure S5) occurred in the suspension obtained by mixing the

https://doi.org/10.1021/acs.langmuir.3c00297
Langmuir 2023, 39, 6780−6793

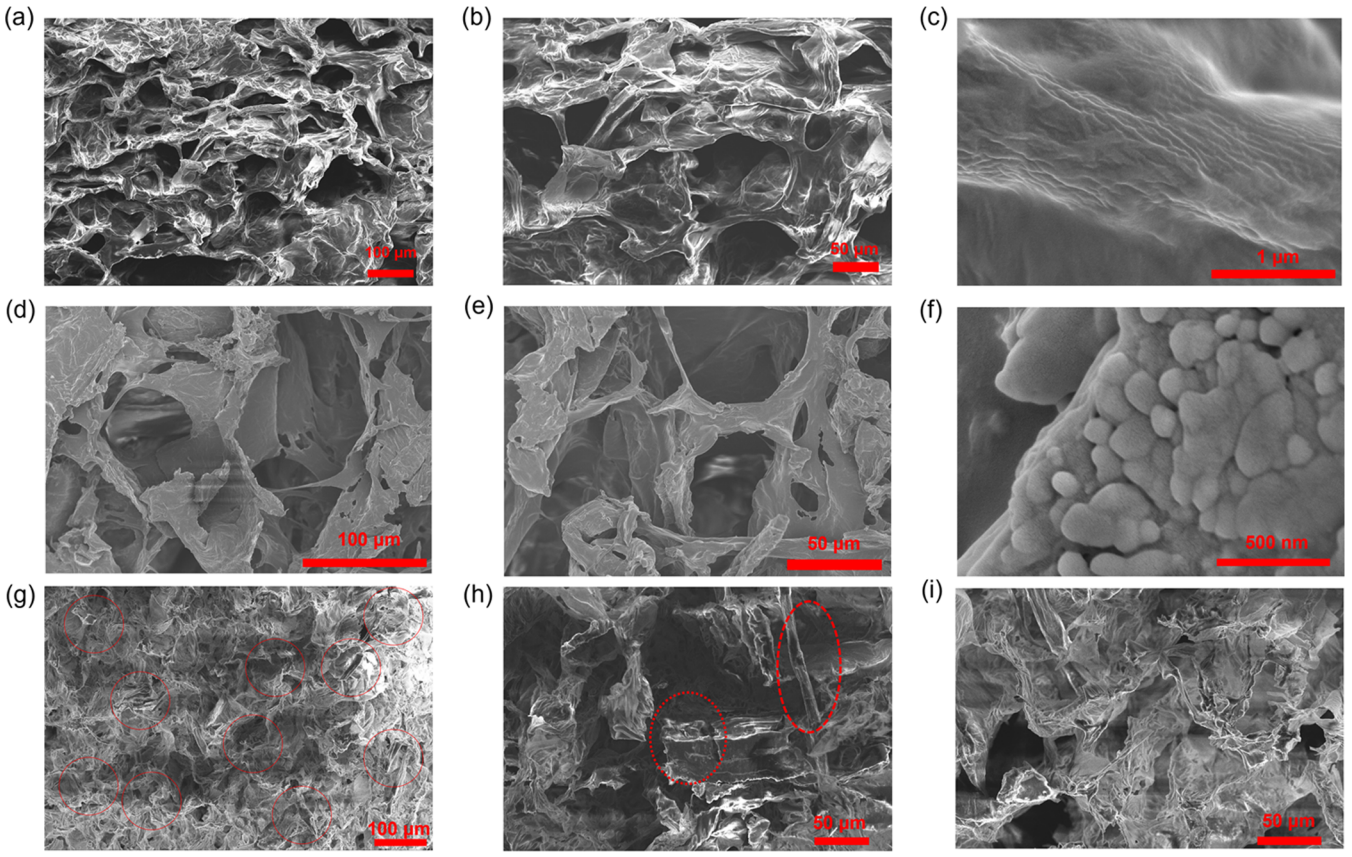

Figure 3. SEM images of the sugarcane bagasse fiber-based aerogel (SBF aerogel) material: (a) 3D interconnected porous structure of the SBF aerogel with the pore size in the range of 20−100 μm, (b) porous structure, and (c) wall surface in the porous structure. SEM images of the SBFAP material: (d) 3D interconnected porous structure of the SBFAP with the pore size from 20 to 100 μm, (e) porous structures, and (f) wall surface in the porous structure, which exhibited a layer of complexes between the Fe^{3+} ions and TA, (g−i) Cross-sectional images of the SBFAP, in which the red areas (SBF) with a diameter range of 6−10 μm were randomly distributed in the material interior.

TA@SBF solution with PVA@Fe(III). This phenomenon can be explained by the fact that the TA molecules at a high concentration created H-bonds with -OH groups of PVA, hence reducing the concentration of free PVA in the mixed solution. Consequently, PVA did not form hydrogen bonds with the cellulose in the SBF to form the suspension. Therefore, the TA concentration of 3−6 mg/mL was considered suitable for the fabrication of the SBFA material.

Characterization of the SBFAP. The morphologies of the SBF aerogel and the SBFAP material as well as their internal microstructures were investigated with an SEM system. The surface structure of the SBF aerogel was observed as shown in Figure 3a−c, which exhibited that the material has 3D interconnected pore structures with a pore size from 20 to 100 μm and a pore wall thickness of less than 1 μm.[14,24] As a result, the aerogel had a low density (0.0495 g/cm^3) and a high porosity (96.7%), which is predicted in Note S1.[43,45] The specific surface area of the SBFAP material was 17.3 m^2/g, which was comparable to those of the reported aerogel materials. Thus, there were main factors that reduced the thermal conductivity of the SBF aerogels.[13,30] The surface morphologies of the SBFAP aerogel were observed as shown in Figure 3d−f. It was observed that the SBFAP material also possessed 3D interconnected porous structures with the similar pore size and pore wall thickness. Additionally, the formation of TA@Fe^{3+} complexes by the crosslinking of -OH groups of TA and Fe^{3+} ions was observed at the pore walls of the SBFAP material (Figure 3f), and the particle sizes of complexes were varied in the range of 50−200 nm. The complex particles were distributed in a layer with a high particle density, leading to an enhancement in the light absorbance of the SBFAP material. Besides, the multiple reflections of light in microporous structures of the SBFAP are also attributed to enhancing the light absorption ability. Figure 3g−i exhibits the cross-sectional SEM images of the SBFAP material. It can be observed that there are red areas in Figure 3g with a diameter range of 6−10 μm randomly distributed in the SBFAP interior. This structure of SBFAP was similar to that of the fiber-reinforced composite. Since the SBF played the role of the reinforcing material, the mechanical stability of the SBFAP was enhanced. Besides, it is clear from the cross-sectional SEM image that the SBFAP also had vertically oriented porous structures, facilitating the water transportation into the pores. This is an important property of the photothermal material.

Comparison of the raw SBF and the treated SBF regarding the chemical composition: The XRD pattern of the raw SBF presented two peaks (narrow diffractions) with a low intensity at the 2-θ (degree) of around 20.2 and 24.7° as shown in Figure 4a. In contrast, three well-defined crystalline peaks, observed at the 2-θ (degree) of around 15−16, 21−22, and 35°, were typical in the XRD pattern of the treated SBF (Figure 4a).[46] These peaks were more intense and sharper than those of the raw SBF. In addition, the crystalline index, which was calculated from the XRD pattern, of the treated SBF

https://doi.org/10.1021/acs.langmuir.3c00297
Langmuir 2023, 39, 6780−6793

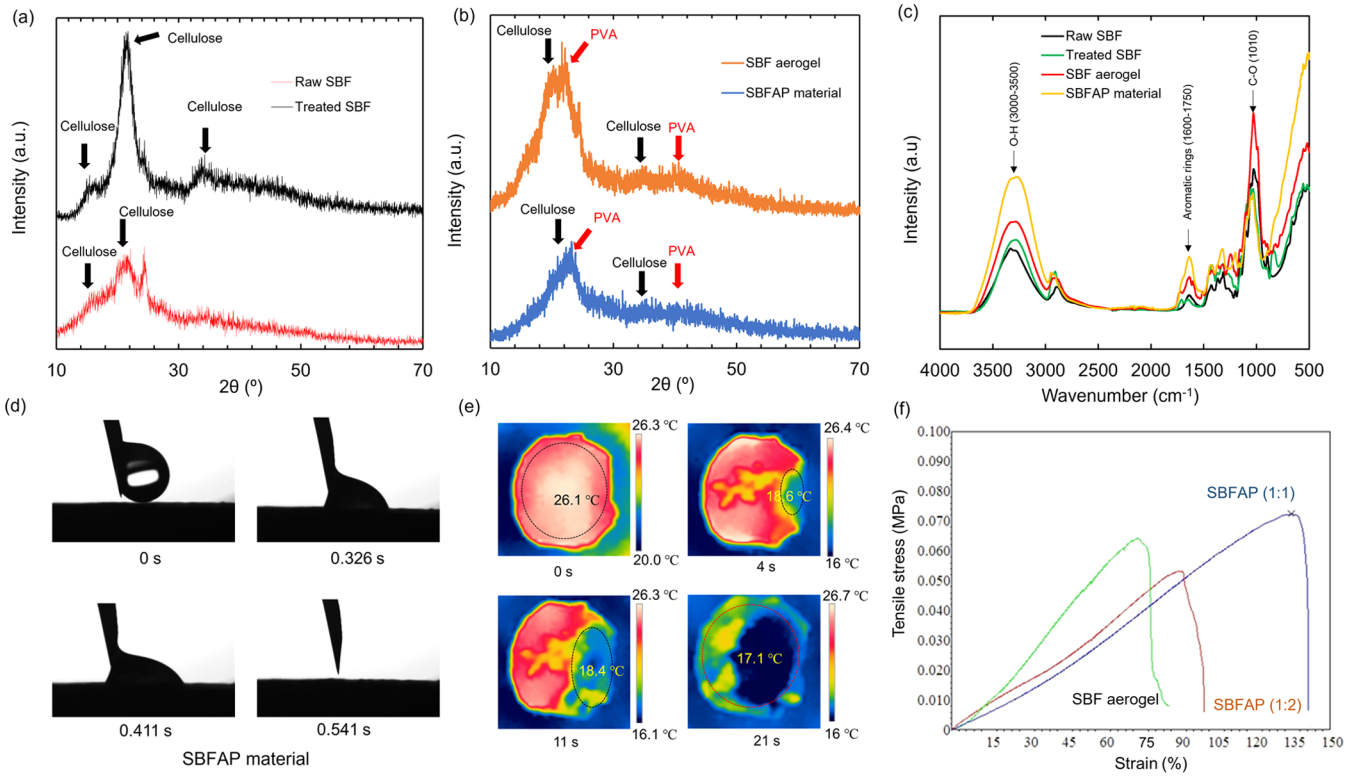

Figure 4. XRD spectra of (a) raw SBF and the treated SBF and (b) SBF aerogel and SBFAP material. (c) FTIR spectra of the raw SBF, the treated SBF, the SBF aerogel, and the SBFAP material. (d) Photographic images of the SBFAP's contact angles and water droplet permeation processes. (e) Water transmission ability of the 20 mm-thick SBFAP material (SBFAP2), which indicated that water could be transported from the SBFAP bottom to the evaporation surface within 4 s. (f) Stress−strain curves of the SBF aerogel and the SBFAP SBFAP (1:2) and SBFAP (1:1) material.

(56.68%) was higher than that of the raw SBF (35.42%), which was almost similar to the reported results.[43,44] Figure S6 displays the XRD patterns of the treated SBF and the SBF aerogel. Unlike the XRD pattern of the treated SBF, in the XRD pattern of the SBF aerogel, the characteristic peaks of PVA at around 23 and 42° could be observed.[47] The result suggested the presence of PVA in the aerogel and the formation of crosslinking between PVA and cellulose in the SBF. Figure 4b displays the XRD pattern of the SBFAP material. Accordingly, the SBFAP material exhibited diffraction peaks at the same positions but with lower intensities as compared to the SBF aerogel. This can be attributed to the presence of TA@Fe^{3+} complexes in the SBFAP structure.[20]

The composition of functional groups in the materials was determined using FTIR analysis, as shown in Figure 4c, which presented that the position and the intensity of peaks in the FTIR spectra of the raw SBF and the treated SBF were almost the same. As cellulose was the main component of both materials, its characteristic peaks at the wavenumber of 1570 (C═C vibration), 1480 (C−H stretching vibration), 1010 (C−O stretching vibration), and 875 (C−C stretching vibration) cm^{-1} could be observed.[43,46] The characteristic peaks in the range of 1600−1700 cm^{-1}, corresponding to the C═O vibration of aromatic rings in lignin, remained after the raw SB treatment. The broadband vibration peak in the range of 3000−3500 cm^{-1} corresponded to the stretching of the hydrogen bond (-OH group) of the cellulose in the SBF. It was found that the SBF aerogel had the same FTIR spectrum as the SBF.[20] Since PVA contained C−C, C−H, and O−H-bonds, the presence of PVA in the SBF aerogel resulted in a slight increase in the intensity of peaks corresponding to the vibration of functional groups such as C−C, C−H, and O−H in the FTIR spectrum of the SBF aerogel. Meanwhile, the major differences in the FTIR spectrum between the SBFAP and the SBF aerogel were that (1) the wavenumber of the peaks of the SBFAP was shifted slightly compared to that of the SBF due to the presence of the Fe^{3+}-containing complexes and (2) the intensity of peaks at the wavenumber range of 1600−1700 cm^{-1} of the SBFAP was higher than that of the SBF aerogel (Figure 4c), due to the influence of aromatic rings in the TA, which built up the SBFAP material.[41] Similar to the XRD analysis result, the stretching vibration of the TA@Fe^{3+} complexes could not be identified in the FTIR spectrum of the SBFAP. However, the FTIR spectrum indicated that the SBFAP possessed numerous hydrophilic groups, such as O−H and C=O, thus enhancing the SBFAP's hydrophilicity.

EDS analysis was performed to investigate the elemental composition of the SBF aerogel and the SBFAP material. The elemental percentages of these samples are shown in Table 2. It is indicated that C and O were the main constituents of the SBF aerogel, accounting for 65.99 and 34.01%, respectively. This is because C and O elements are the main constituents of the SBF, PVA, and other organic substances (e.g., lignin,

Table 2. Percentages of Elements in the SBF Aerogel and SBFAP Materials

	composition (at %)		
sample	C	O	Fe
SBF aerogel	65.99	34.01	
SBFAP sample	45.12	41.92	6.62

https://doi.org/10.1021/acs.langmuir.3c00297
Langmuir 2023, 39, 6780−6793

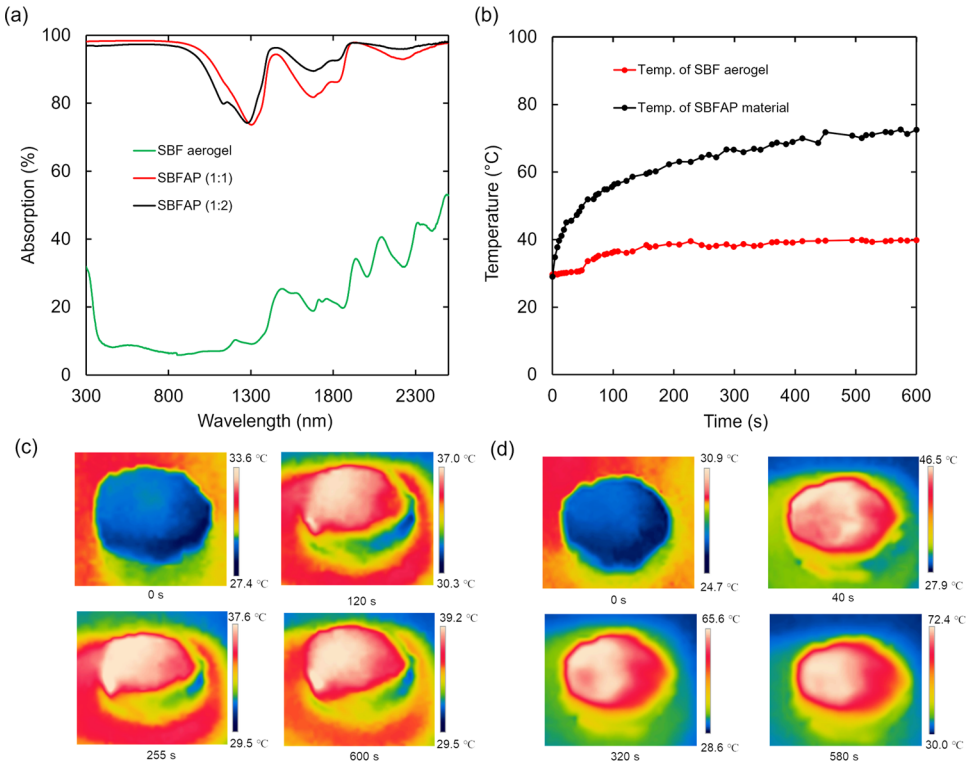

Figure 5. (a) UV−vis−NIR absorption spectra of the SBF aerogel and the SBFAP, indicating that the average light absorbance of the SBFAP material in the wavelength range of 300−950 nm was approximately 97%. (b) Curves of the change in temperature over time of the SBF aerogel and the SBFAP material. (c, d) IR images of the SBF aerogel and the SBFAP material surfaces at different times, respectively.

hemicellulose) in the SBF. In contrast, for the SBFAP material, in addition to C (45.12%) and O (41.92%), the presence of Fe (6.62%) and Cl (6.34%) was also verified. The results also exhibited that the nanoparticles formed on the pore wall surface in the SBFAP, as shown in Figure 3f, were the complexes between Fe^{3+} ions and TA. Besides, the observation of the Cl element in the EDS spectrum of the SBFAP was due to the utilization of $FeCl_3{\cdot}6H_2O$ in the material fabrication.

The water transportation ability plays an essential role in sustaining water evaporation in the SSG system. Therefore, the wetting behaviors of the SBF aerogel and the SBF aerogel-based photothermal material were investigated by measurement of water contact angles. As shown in Figures 4d and S7, while the SBF aerogel completely absorbed 18 μL of water droplets (Figure S7) within 3.75 s, the water droplets could rapidly permeate into the SBFAP material (Figure 4d) in 0.541 s. The increase in the water permeation rate of the SBFAP can be explained by the presence of TA with numerous hydrophilic -OH groups, which enhanced the hydrophilic properties of the SBFAP material. Then, a 20 mm-thick SBFAP piece was placed on the water surface to identify the water transportation ability of the SBFAP material. Water could be transferred from the SBFAP bottom to the evaporation surface within 4 s (the surface temperature declined from 26.1 to 18.6 °C due to the cooling effect) and then completely wetted the top surface in about 21 s (the temperature of the SBFAP surface reduced to 17.1 °C), resulting in a fast water transportation rate (0.95 mm/s) as shown in Figure 4e.[14,28] Moreover, the rapid water swelling of the SBFAP verified its excellent water transport ability as shown in Video S1. The results indicated that the SBF aerogel and the SBFAP material had hydrophilic properties with near-zero contact angles and excellent water transportation abilities. This can be attributed to (1) their interconnected porous structures with the pore size range of 20−100 μm, thus creating their rough surface, and (2) the presence of numerous hydrophilic groups on their surface and interior.[37]

Mechanical Property of the SBFAP. The mechanical performance of the SBF aerogel and the SBFAP material was characterized using a servo control system universal testing machine. The obtained tensile stress−strain and compressive stress−strain curves are displayed in Figures 4f and S8. It can be seen that the SBF aerogel and the SBFAP material exhibited high ultimate tensile strengths, the values being 53 and 64 kPa, respectively.[48] The ultimate tensile strengths of the fabricated materials were equivalent to those of other aerogels.[42−44] This can be attributed to the hydrogen bonds between PVA and CFB, which produced the tight crosslinked system, thus enhancing the reinforcement capability. Compared to the SBF aerogel, the SBFAP material had a greater ultimate tensile strength thanks to the presence of TA in its composition. The TA, containing numerous -OH groups with high polarity, could form more crosslinked bonds directly with PVA and CFB in the SBFAP fabrication. As a result, the ultimate tensile strength of the SBFAP material could be improved. Figure 4f and Table 1 show that the ultimate tensile strength of the SBFAP was elevated from 64 (SBFAP 1:2) to 72 kPa (SBFAP 1:1) with increasing concentration of TA from 3 to 6 mg/mL. This implied that using the optimal TA concentration could improve the ultimate tensile strength of the SBFAP. Figure S8 illustrates the compressive strength−strain curves of the SBF aerogel and the SBFAP material. It was found that both the compressive and tensile strengths of the SBFAP were higher than those of the SBF aerogel. Moreover, the SBFAP material

https://doi.org/10.1021/acs.langmuir.3c00297
Langmuir 2023, 39, 6780−6793

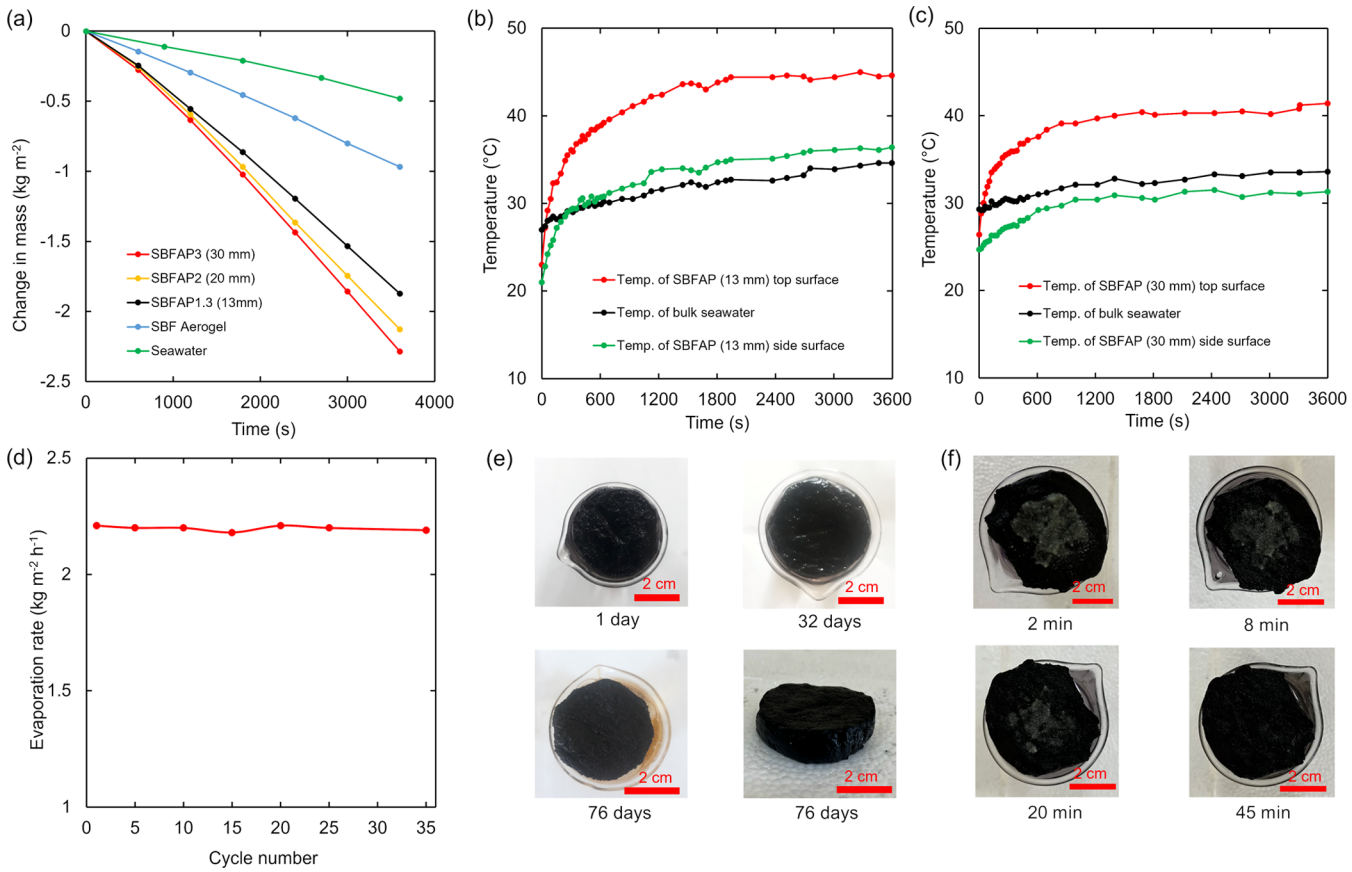

Figure 6. (a) Mass change of the blank seawater, SBF aerogel, SBFAP1.3 (thickness of 13 mm), SBFAP2 (thickness of 20 mm), and SBFAP3 (thickness of 30 mm) materials under 1 sun illumination. The curves illustrate changes in the temperature over time of the top and side surfaces of the SBFAP material and the bulk water in the SSG system based on (b) SBFAP1.3 and (c) SBFAP3 materials. (d) Seawater evaporation rate in the SBFAP3 cycle test under 1 sun with 1 h for each cycle. (e) Long-term stability test with the seawater under real conditions for 76 consecutive days. (f) Salt dissolution process on the SBFAP surface.

could be compressed easily and returned to its original shape as shown in Videos S1 and S2. These results indicated that the SBFAP material had suitable mechanical properties to be applied in the SSG systems under outdoor conditions. Besides, the SBFAP material for application in the SSG system was fabricated with the same ratio of ingredients as the SBFAP (1:1) material.

Thermal Behavior of the SBFAP Material. The thermal management of photothermal materials to minimize heat energy loss plays a critical role in enhancing the water evaporation capacity of SSG systems.[18] However, it is difficult to reduce heat loss from convection and radiation heat. The heat loss from conduction of heat to the surrounding environment depends on the nature of the photothermal material, particularly thermal conductivity. Low thermal conductivity is a critical factor in reducing energy loss via conduction of heat and enhancing the solar energy conversion efficiency. The thermal conductivity of the SBFAP material, identified with a thermal conductivity measurement system, was 0.084 and 0.137 W m^{-1} K^{-1} in the dry and wet states, respectively.[22] In the wet conditions, the porous structure of the SBFAP material was filled with water molecules, resulting in its higher thermal conductivity. However, the SBFAP material exhibited low thermal conductivities in both dry and wet conditions. This is because of its high porosity (95.3%), low density (0.0705 g/cm^3), and 3D interconnected porous structure that formed air-filled chambers, thus preventing the heat conduction.[13,17]

In an SSG system, the heat energy for water evaporation is generated by the photothermal material, which absorbs solar energy. A material with higher light absorption ability can enhance the solar energy conversion and reduce the heat loss via reflection. The light absorption ability (A) of a photothermal material was calculated based on its scattering reflectance (R) and transmittance (T). The SBF aerogel had a low light absorption ability, the value being around 30%, as shown in Figure 5a. Compared to the SBF aerogel, the SBFAP material demonstrated a higher absorbance in the wavelength range of 300−2500 nm. Particularly, the average light absorption of the SBFAP material was approximately 97 and 94% in the wavelength range of 300−950 and 1350−2500 nm, respectively (Figure 5a). The light absorption spectra of the SBFAP (1:2) and SBFAP (1:1) materials were quite similar, which are named in Table 1, suggesting that the mechanical stability of the photothermal materials could be improved by varying the concentration of TA, without adverse impacts on their light absorption ability. The high sunlight absorption of the SBFAP material may result from two major factors: (1) the complex layer of Fe^{3+} ions and TA had excellent ligand-to-metal transitions[41] and (2) the complex micro/nanoparticles on the surface (Figure 3f) and the rough and microporous structure of the SBFAP material (Figure 3d) could induce multiple light reflections on the SBFAP surface.[22,49] To

https://doi.org/10.1021/acs.langmuir.3c00297
Langmuir 2023, 39, 6780−6793

investigate the heat generation capabilities of the SBF aerogel and the SBFAP, both samples were placed under 1 sun conditions (1 kW m^{-2}) and the changes in their surface temperatures were monitored with an IR camera. As depicted in Figure 5b, a speedy elevation in the SBFAP surface's temperature from 30 to 50 °C was observed in less than 70 s, followed by a gentle increase to approximately 73 °C in 500 s. On the contrary, the SPF aerogel's surface temperature showed a gradual increase before getting stable at around 39 °C after 600 s (Figure 5b,c). Besides, the IR images of the SBFAP material also indicated that its temperature was rapidly increased under 1 sun conditions (Figure 5d). It was observed that the SBFAP material had an outstanding photothermal conversion capability. The attained results proved that the SBFAP material had high light energy conversion and excellent thermal insulation. These are critical properties for improving the performance of the SSG system based on the SBFAP material.

Solar Evaporation Performance under Indoor Conditions. To assess the water evaporation rate of the SBFAP material, 4.2 cm-diameter SBFAP pieces with various thicknesses (Figure S9) were combined with a polyethylene foam to fabricate an SSG system as shown in Figure 1 (Figure S10).[20] The structure was floated on the seawater contained in a beaker. To investigate the evaporation behavior of the SBFAP at indoor conditions, the evaporation experiments were conducted under 1 sun conditions for 60 min, and the mass changes of the seawater were observed using an electronic balance. As illustrated in Figure 6a, the seawater evaporation rates of the 13 mm-thick SBF aerogel and the 13 mm-thick SBFAP were 0.967 and 1.87 kg m^{-2} h^{-1}, respectively, which were about 2 and 4.15 times higher than those of the seawater (0.45 kg m^{-2} h^{-1}) without any absorbers. When the thickness of the SBFAP material was 13 (SBFAP1.3), 20 (SBFAP2), and 30 mm (SBFAP3), the evaporation rate of the SBFAP material was improved from 1.87 to 2.13 and then 2.28 kg m^{-2} h^{-1}, (Figure 6a). Moreover, Figure S12a presents the water evaporation rate with error bars, indicating that the SSG system's evaporation rate was also dependent on the indoor conditions during the experiments, such as room humidity and temperature.[22] The increase in the water evaporation performance at a higher thickness of the SBFAP could be attributed to (1) the increased side surface area, leading to the enhanced water evaporation area (steam escape area)[30] and (2) the heat harness from the surrounding environment and bulk water by the side surface.[7,11,13] Since the SBFAP material had a low thermal conductivity in the wet conditions (0.137 W m^{-1} k^{-1}), its thermal insulation property could be improved with increasing thickness. As a result, the temperature of SBFAP's side surface under 1 sun illumination was lower than that of the bulk water and the ambient air. Therefore, the heat energy from the bulk water and the surrounding environment could be harnessed to evaporate seawater on the SBFAP side surface.[11]

To verify this assumption, the top surface and side surface temperatures of the SBFAP material (with a thickness of 13, 20, and 30 mm) as well as the bulk seawater temperature were monitored under 1 sun illumination conditions as presented in Figure 6b,c. The changing temperature exhibited that the surface temperatures of all samples with different thicknesses were increased rapidly from 23 to 26 °C before being stable at approximately 41−42 °C (Figures 6b,c and S11). In contrary, the bulk seawater temperature during the evaporation process was increased slowly from 27 to 28 °C before reaching approximately 34.6 °C and 33.6 °C for the SBFAP1.3 and SBFAP3, respectively (Figure 6b,c). It is clear that the bulk seawater temperature decreased as the SBFAP thickness increased, indicating that the heat loss due to the heat conduction from the top surface to the bulk seawater also declined. This led to an increase in the heat utilization efficiency at the air−water interface.[11,25] When the material thickness was 13 mm, as shown in Figure 6b, the temperature of the side surface of the SBFAP material was lower than that of the bulk water during the first 300 s after illumination. In this period, the heat conduction loss from the SBFAP surface was transmitted only to the interior of the SBFAP material, heating the SBFAP's side surface. However, it did not reach the bulk water surface. After 300 s of illumination, the temperature of the SBFAP's side surface was gradually increased, being higher than that of the bulk water (Figure 6b). The results suggested that a part of the conduction heat from the SBFAP surface was transmitted to the bulk water and became the heat conduction loss. This led to an increase in the temperatures of the bulk water and the side surface of the SBFAP material. This also implies that the 13 mm-thick SBFAP material was inefficient in harnessing the heat energy from the bulk seawater and the surrounding environment for water evaporation. For the SBFAP2 (20 mm) and SBFAP3 (30 mm) samples, Figures S11(b) and 6c shows that the temperatures of their side surfaces were consistently lower than that of the bulk water.[11,25] The results indicated that the heat conduction from the SBFAP material's surface could be retained mainly on its side surface, which was then used for water evaporation.[11,25] This was a main factor to reduce the bulk water temperature. In addition, as the material thickness increased, the light intensity at the bulk water surface decreased due to the higher distance between the light source of solar simulation and the bulk water surface, leading to a decline in the temperature of the bulk water. It also indicated that with thicker SBFAP materials, the thermal energy from the bulk water was transferred to the SBFAP's side surface. In other words, the heat from the bulk seawater was harnessed for water evaporation. Moreover, the changes in temperature in the SSG systems based on SBFAP1.3 and SBFAP3 materials under 1 sun were shown by IR images at different times (Figure S11a). It can be seen that the SBFAP's side surface temperature was always lower than that of the surrounding environment when the water evaporation experiment was conducted under 1 sun illumination. As a consequence, the side surface of the SBFAP3 material could also utilize the heat energy from the surrounding environment for water evaporation.[25] This was an essential factor to enhance the water evaporation rate.

The energy conversion efficiency (η_{eq}, %) can be calculated by the following equation[13,20]

$$\eta_{eq} = \frac{\Delta m h_{LV}}{I} \quad (1)$$

where Δm is the evaporation rate of seawater under 1 sun (the unit of Δm is kg m^{-2} h^{-1}), h_{LV} is the enthalpy for the liquid vapor phase change in the SBFAP material (J g^{-1}), and I is the energy intensity of the incident light (1 kW m^{-2}). To explore benefits of applying the SBFAP in the evaporation process and identify the seawater evaporation enthalpy in the SBFAP material, the seawater evaporation performance in the SSG system under the dark conditions was evaluated. The

https://doi.org/10.1021/acs.langmuir.3c00297
Langmuir 2023, 39, 6780−6793

evaporation rates of the seawater without the SBFAP material, the SSG system using the 13 mm-thick SBF aerogel, and the SSG system using the 13 mm- and 30 mm-thick SBFAP were 0.078, 0.133, and 0.155 kg m^{-2} h^{-1} (Figure S12b), respectively, exhibiting that the water evaporation rates of the SSG systems based on the aerogel materials were higher than that of the blank seawater. This is because the evaporation performance of the SSG system solely relied on the seawater evaporation enthalpy of the photothermal material in dark conditions. In other words, the decrease in the seawater evaporation enthalpy of the SBFAP material was responsible for the increase in the performance of the SSG system. Besides, the evaporation rate of the 30 mm-thick SBFAP was 0.155 kg m^{-2} h^{-1}, slightly higher than that of the 13 mm-thick SBFAP (Figure S12b). Hence, in the case of dark evaporation, since the light was not absorbed on the SBFAP's surface, the temperatures of the top and side surfaces of the photothermal material as well as the bulk water surface were not changed. Therefore, the water evaporation rate mainly depends on three factors as follows: (i) heat harvest from the bulk water and environment for water evaporation,[11] (ii) the reduced enthalpy of water evaporation,[13] and (iii) the exposed side surface of the SBFAP material. Besides, the light-to-heat conversion ability of the SBFAP material under solar illumination was an extremely important factor to enhance the water evaporation rate of the SSG system. For this reason, the performances of the SSG systems based on SBFAP samples were almost the same. However, the SBFAP3 demonstrated a higher water evaporation rate compared to that of the SBFAP1.3 as a result of its larger side surface area.

The decline in the seawater evaporation enthalpy of the SBFAP material can be explained by the interaction of numerous hydroxyl groups on the PVA, cellulose of the SBF, and TA, which were used to fabricate the SBFAP. Hydrophilic groups in the interconnected porous structure of the SBFAP activated and transferred water molecules into the material interior, subsequently formed hydrogen bonds, and generated intermediate water in the SBFAP material. As a consequence, the overall energy demand of water evaporation was reduced.[7,13] The seawater evaporation enthalpy values at different conditions were calculated using the formula (2)[13,17]

$$\Delta H_0 m_0 = \Delta H_1 m_1 \quad (2)$$

where ΔH_0 (2450 J g^{-1}) and ΔH_1 are the evaporation enthalpy values of the seawater at different conditions and m_0 (0.078 kg m^{-2} h^{-1}) and m_1 (0.155 kg m^{-2} h^{-1}) are the mass changes of seawater in the dark evaporation experiments. Therefore, the seawater evaporation enthalpy in the SBFAP material was estimated to be as high as 1232 J g^{-1}, which was lower than that in the blank seawater. This was a vital property of the SBFAP photothermal material to enhance the performance of the SBFAP-based SSG system. To compare with the calculated evaporation enthalpy, the evaporation enthalpy of water in the SBFAP material was also measured with differential scanning calorimetry (DSC) at a temperature range from 30 to 130 °C and a heating rate of 5 K min^{-1}. The DSC results exhibited that the vaporization enthalpy of water in the SBFAP was 1353 J g^{-1}, the value being lower than that of free water (2438 J g^{-1}), as shown in Figure S13. This finding is consistent with the previous report regarding the vaporization enthalpy of free water.[13] The vaporization enthalpy of water in the SBFAP measured with DSC (1353 J g^{-1}) was almost equivalent to that calculated with formula (2) (1232 J g^{-1}). The difference between both values was due to errors in determining the surface area of the SBFAP material and the mass change of water in the evaporator under dark conditions.

The mass change of seawater in the SBFAP materials, including SBFAP1, SBFAP2, and SBFAP3, under 1 sun was 1.87, 2.13, and 2.28 kg m^{-2} h^{-1} (Figure 6a), respectively. The energy conversion efficiencies of the SSG systems were 61.3, 70.2, and 75.3%, respectively. To clarify the thermal management in the SBFAP-based SSG system, an analysis of the heat loss during the evaporation process was conducted.[7,13] As shown in Note S2, the total heat loss, including heat loss via conduction (4.6%), radiation (5.4%), convection (4.1%), and reflection (5%), accounted for approximately 19.1%. Therefore, the heat energy for evaporation and the heat loss accounted for 94.4% of the input energy. This may result from errors in the temperature measurement as well as the calculation of the seawater evaporation enthalpy and the SBFAP surface area. In comparison with other materials (e.g., biomass, aerogel materials, polymer materials, and carbon-based photothermal materials) in Table S1, the SBFAP material exhibited a similar or even higher water evaporation rate and energy conversion efficiency. It also possessed a superior structural durability compared to other biomass-based photothermal materials.

Structural Stability of the SBFAP Material. The stable and high seawater evaporation efficiency is a crucial property for the actual application of the SBFAP photothermal material. Thus, the SBFAP's stability was assessed by conducting a cycle test under 1 kW m^{-2} illumination within 60 min for each cycle. As shown in Figure 6d, the stability test was performed over 35 cycles for 2 weeks in the 30 mm-thick SBFAP-based SSG system. It was found that the water evaporation rate slightly fluctuated around 2.28 kg m^{-2} h^{-1}, showing that the SBFAP was a durable photothermal material. The mass change of water in each cycle was the result of variations in the ambient temperature and humidity during the experiment. After 35 cycles, salt crystallization could not be observed on the SBFAP top surface. The iron concentrations (Fe^{3+} and Fe^{2+}) in the original seawater and the seawater soaked with the SBFAP material for 120 h were determined to be 0.636 and 67.58 mg/L, respectively. This implied that the Fe^{3+} ions were released into the seawater from complexes of Fe^{3+} and TA in the SBFAP material. Additionally, when the SBFAP material was placed on the surface of seawater contained in a beaker for 76 consecutive days in real conditions, no change in the color of the SBFAP surface was observed (Figure 6e).[33] The structural stability of the SBFAP material was ascribed to the synergistic effect of the strong H-bond interactions between the SBF, TA, and PVA and the coordination between the TA and Fe^{3+} ions. Besides, the morphologies of the top surface and interior structure of the SBFAP material were examined using SEM analysis (Figure S14), indicating that only a small amount of salt crystals was accumulated on the pore walls (Figure S14a), whereas salt crystals could not be found in the SBFAP's interior structure (Figure S14b). Consequently, the water transportation to the top surface of the SBFAP did not interfere. This demonstrated that the SBFAP had an excellent self-cleaning ability, thanks to its rapid water transportation (0.9 mm/s) and the 3D porous structure. The salt-resistant antifouling property of the SBFAP was investigated by placing 1 g of commercial salt onto the SBFAP top surface, which was put in a seawater-containing beaker. The salt crystals quickly dissolved after 2 min and diffused back to the bulk seawater

https://doi.org/10.1021/acs.langmuir.3c00297
Langmuir 2023, 39, 6780−6793

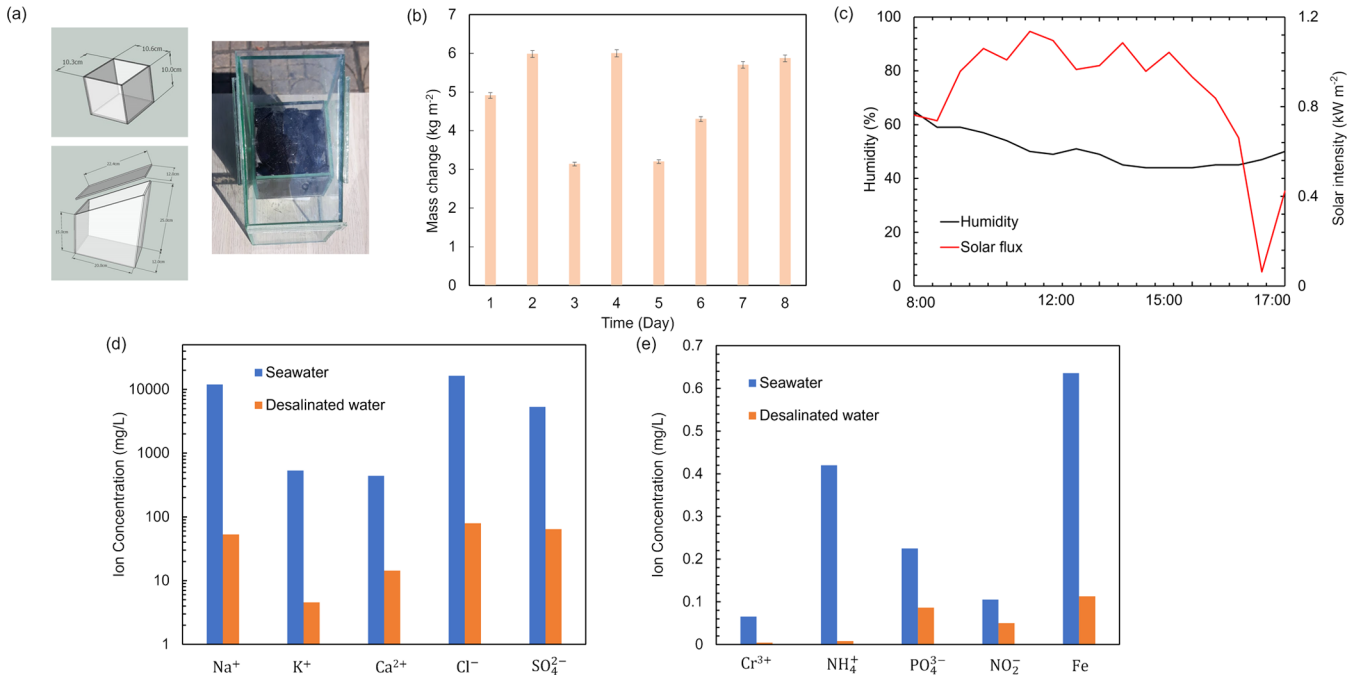

Figure 7. (a) Simple device to perform the solar desalination. (b) Mass of fresh water from the solar desalination device in Hanoi, Vietnam, May–June 2022. (c) Solar intensity and air humidity during solar desalination on day 2. (d, e) Concentrations of main ions (Na^+, K^+, Ca^{2+}, Cr^{3+}, Fe, (including Fe^{3+} and Fe^{2+}) Cl^-, SO_4^{2-}, NH_4^+, PO_4^{3-}, NO_2^-) in the raw and desalinated seawater.

after 45 min via the 3D interconnected porous structure of the SBFAP material, as exhibited in Figure 6f. In other words, the 3D porous structure with the pore size in the range of 20–100 μm enabled excellent transport of water into the SBFAP material, accelerating the transportation of seawater from the bottom to the top surface of the SBFAP for dissolving the accumulated salt crystals. This is why salt crystals could not be seen on the SBFAP surface after the long-term performance of the SSG system.

Solar Desalination under Outdoor Conditions. To verify the solar desalination performance of the SBFAP-based SSG system under real conditions and evaluate the desalinated water quality, the seawater purification test was performed and is presented in Figure 7a. The dimensions of the desalination device used for the test are also displayed in Figure 7a. Accordingly, the area of the SBFAP in the device was 100 cm^2, whereas the material thickness was in the range of 13–20 mm. The SBFAP material was placed on the surface of seawater in a container, which was covered with a piece of transparent glass for water steam condensation. The desalination performance was characterized in both sunny and cloudy days for 9 h (from 8:00 to 17:00) in Hanoi, Vietnam. The solar intensity and humidity during the desalination process were monitored as shown in Figure 7c. The desalination device produced a stable amount of clean water under different conditions. While 5.8 L of fresh water was collected in the sunny days (days 2, 4), the clean water volume was reduced in the cloudy days (Figure 7b).[13,17] This can be attributed to the higher average sunlight intensity (0.77 kW m^{-2}) in the sunny days. However, the water collection efficiency in real conditions was lower than the evaporation efficiency in the experimental conditions because of the following reasons: (1) sunlight intensity attenuation due to the partial absorption of the glass and water droplets, which were condensed on the glass's inner surface (Figure S15), (2) unstable outdoor conditions (Figure 7c), and (3) incomplete condensation of the generated steam.[20] The concentrations of ions (Na^+, K^+, Ca^{2+}, Cr^{3+}, Fe^{3+} and Fe^{2+}, Cl^-, SO_4^{2-}, NH_4^+, PO_4^{3-}, NO_2^-) in the seawater before and after evaporation were determined (Figure 7d). It can be seen that the desalination device could achieve 99.99% ion rejection, resulting in all ion concentrations being lower than the WHO standards.[50] Therefore, the water desalinated by the purification device can be considered sufficiently clean for human consumption. The desalinated water production capacity of the systems can be improved by increasing the area of the SBFAP photothermal material and placing the desalination device in higher light intensity conditions. By doing so, the developed SBFAP-based SSG system can meet household needs for clean water. The fabrication cost of the SBFAP photothermal material was estimated to be approximately 2 USD (Table S2). Hence, the natural cellulose fiber-derived SBFAP photothermal material has high potential for practical application to purify seawater.

CONCLUSIONS

In this work, the sugarcane bagasse fiber aerogel-based photothermal (SBFAP) material was fabricated by forming hydrogen bonds between SBF, PVA, and TA. The SBF-derived aerogel was reinforced like a composite material, showing excellent mechanical properties. The developed SBFAP demonstrated a high light absorption capacity (94%). With the 3D interconnected porous microstructure, the SBFAP could enhance water transportation ability (0.9 mm/s), reduce thermal conductivity (0.084 W m^{-1} K^{-1}), and dissolve the accumulated salt crystals. The presence of numerous hydroxyl groups in the porous microstructure lowered the seawater evaporation enthalpy. By transferring the ambient heat in evaporation, the SBFAP could achieve a seawater evaporation rate of 2.28 kg m^{-2} h^{-1} and an energy conversion efficiency of 75.3% under 1 sun. At realistic conditions, the solar desalination device produced freshwater that meets the

https://doi.org/10.1021/acs.langmuir.3c00297
Langmuir 2023, 39, 6780–6793

WHO's standards for drinking water. Especially, the SBFAP photothermal material presented excellent structural stability and high salt tolerance, which were evidenced by the high desalination performance for at least 76 days of continuous evaporation under real conditions. This study provides an innovative strategy to fabricate a sustainable, low-cost, and green photothermal material, which can be used in SSG systems for seawater desalination.

■ ASSOCIATED CONTENT

Supporting Information

The Supporting Information is available free of charge at https://pubs.acs.org/doi/10.1021/acs.langmuir.3c00297.

Pretreatment of sugarcane bagasse fibers, fabrication of the aerogel based on the SBF, proposed chemical structures for H-bonding and complexes between Fe^{3+} and hydroxyl groups of TA in the SBFAP material, fabricated SBF aerogel and SBFAP material, exploration of the photothermal material preparation conditions, XRD patterns of the SBF aerogel and the treated SBF, contact angles and water droplet permeation process in the SBF aerogel, compressive strength−strain curves of the SBF aerogel and the SBFAP material, SBFAP materials with a thickness of 13, 20, and 30 mm, schematic illustration of the SSG system under indoor conditions, temperature changes of the top surface and the side surface of the SBFAP material, mass change of the SSG system based on the SBFAP material under dark conditions, SEM images of the SBFAP material after 76 consecutive days of evaporation under real conditions, and thermal loss analysis (PDF)

Rapid water swelling of the SBFAP (MP4)

Mechanical property of the SBFAP (MP4)

■ AUTHOR INFORMATION

Corresponding Author

Tien Thanh Pham − *Vietnam Japan University (VJU), Vietnam National University, Hanoi (VNU), Hanoi 100000, Vietnam;* orcid.org/0000-0001-7507-2429; Phone: (084) 24 7306 6001; Email: pt.thanh@vju.ac.vn

Authors

Hoang Giang Nguyen − *Vietnam Japan University (VJU), Vietnam National University, Hanoi (VNU), Hanoi 100000, Vietnam; Environmental Radioactivity Monitoring & Impact Assessment Center, Institute for Nuclear Science and Technology, Vietnam Atomic Energy Institute, Hanoi 100000, Vietnam*

Thi An Hang Nguyen − *Vietnam Japan University (VJU), Vietnam National University, Hanoi (VNU), Hanoi 100000, Vietnam*

Danh Bich Do − *Faculty of Physics, Hanoi National University of Education, Hanoi 100000, Vietnam;* orcid.org/0000-0002-6004-8044

Xuan Nui Pham − *Department of Chemical Engineering, Hanoi University of Mining and Geology, Hanoi 100000, Vietnam*

Tuan Hong Nguyen − *Center for High Technology Development, Vietnam Academy of Science and Technology (VAST), Hanoi 100000, Vietnam*

Ha Lien Thi Nghiem − *Institute of Physics, Vietnam Academy of Science and Technology, Hanoi 100000, Vietnam*

Minh Viet Nguyen − *VNU Key Laboratory of Advanced Material for Green Growth, Faculty of Chemistry, VNU University of Science, Hanoi 100000, Vietnam*

Complete contact information is available at: https://pubs.acs.org/10.1021/acs.langmuir.3c00297

Author Contributions

T.T.P.: supervision and writing—original draft, review, and editing; H.G.N.: methodology, synthesis, and investigation of the material; T.A.H.N.: investigation, formal analysis, review, and editing; D.B.D.: methodology and writing—draft; X.N.P.: validation and formal analysis; T.H.N.: formal analysis and validation; and H.L.T.N.: formal analysis, data curation, and editing.

Notes

The authors declare no competing financial interest.

■ ACKNOWLEDGMENTS

The main part of this work was performed in the Laboratory of Master's Program in Nanotechnology, VNU Vietnam Japan University.

■ ABBREVIATIONS

SBF, sugarcane bagasse fibers; SBFAP, sugarcane bagasse fiber aerogel-based photothermal; SSG, solar steam generation; PVA, poly(vinyl alcohol); TA, tannic acid; FTIR, Fourier transform infrared spectroscopy; SEM-EDS, scanning electron microscopy with energy dispersive spectroscopy; XRD, X-ray diffraction; UV-Vis-NIR, ultraviolet−visible−near-infrared; IR, infrared; WHO, World Health Organization; PPy, polypyrrole; PEDOT:PSS/NFC, poly(3,4-ethylenedioxythiophene):polystyrene sulfonate/nanofibrillated cellulose; CNT, carbon nanotubes; PDA, polydopamine

■ REFERENCES

(1) Tang, I. N.; Tridico, A. C.; Fung, K. H. Thermodynamic and Optical Properties of Sea Salt Aerosols. *J. Geophys. Res.: Atmos.* **1997**, *102*, 23269−23275.

(2) Abney, C. W.; Mayes, R. T.; Saito, T.; Dai, S. Materials for the Recovery of Uranium from Seawater. *Chem. Rev.* **2017**, *117*, 13935−14013.

(3) Yang, S.; Zhang, F.; Ding, H.; He, P.; Zhou, H. Lithium Metal Extraction from Seawater. *Joule* **2018**, *2*, 1648−1651.

(4) Li, Z.; Xu, X.; Sheng, X.; Lin, P.; Tang, J.; Pan, L.; Kaneti, Y. V.; Yang, T.; Yamauchi, Y. Solar-Powered Sustainable Water Production: State-of-the-Art Technologies for Sunlight-Energy-Water Nexus. *ACS Nano* **2021**, *15*, 12535−12566.

(5) Ahmed, F. E.; Hashaikeh, R.; Hilal, N. Solar Powered Desalination − Technology, Energy and Future Outlook. *Desalination* **2019**, *453*, 54−76.

(6) Wang, Y.; Wu, X.; Yang, X.; Owens, G.; Xu, H. Reversing Heat Conduction Loss: Extracting Energy from Bulk Water to Enhance Solar Steam Generation. *Nano Energy* **2020**, *78*, No. 105269.

(7) Wu, P.; Wu, X.; Wang, Y.; Xu, H.; Owens, G. Towards sustainable saline agriculture: Interfacial solar evaporation for simultaneous seawater desalination and saline soil remediation. *Water Res.* **2022**, *212*, No. 118099.

(8) Ibrahim, I.; Bhoopal, V.; Seo, D. H.; Afsari, M.; Shon, H. K.; Tijing, L. D. Biomass-Based Photothermal Materials for Interfacial Solar Steam Generation: A Review. *Mater. Today Energy* **2021**, *21*, No. 100716.

(9) Wang, F.; Xu, N.; Zhao, W.; Zhou, L.; Zhu, P.; Wang, X.; Zhu, B.; Zhu, J. A High-Performing Single-Stage Invert-Structured Solar Water Purifier through Enhanced Absorption and Condensation. *Joule* **2021**, *5*, 1602−1612.

(10) Lu, Y.; Fan, D.; Shen, Z.; Zhang, H.; Xu, H.; Yang, X. Design and performance boost of a MOF-functionalized-wood solar evaporator through tuning the hydrogen-bonding interactions. *Nano Energy* **2022**, *95*, No. 107016.
(11) Wang, Y.; Wu, X.; Wu, P.; Zhao, J.; Yang, X.; Owens, G.; Xu, H. Enhancing solar steam generation using a highly thermally conductive evaporator support. *Sci. Bull.* **2021**, *66*, 2479−2488.
(12) Pham, T. T.; Dao, T. D.; Nguyen, T. A. H.; Pham, D. D.; Kajikawa, K.; Nguyen, D. C.; Do, D. B.; Nguyen, H. V. Novel Cu and Leaf Nanostructure-Based Photothermal Biomaterial for Efficient Solar Steam Generation. *Adv. Sustainable Syst.* **2021**, *5*, No. 2100159.
(13) Zhao, F.; Zhou, X.; Shi, Y.; Qian, X.; Alexander, M.; Zhao, X.; Mendez, S.; Yang, R.; Qu, L.; Yu, G. Highly Efficient Solar Vapour Generation via Hierarchically Nanostructured Gels. *Nat. Nanotechnol.* **2018**, *13*, 489−495.
(14) Li, J.; Zhou, X.; Jing, Y.; Sun, H.; Zhu, Z.; Liang, W.; Li, A. Ionic Liquid-Assisted Alignment of Corn Straw Microcrystalline Cellulose Aerogels with Low Tortuosity Channels for Salt-Assistance Solar Steam Evaporators. *ACS Appl. Mater. Interfaces* **2021**, *13*, 12181−12190.
(15) Xu, N.; Zhang, H.; Lin, Z.; Li, J.; Liu, G.; Li, X.; Zhao, W.; Min, X.; Yao, P.; Zhou, L.; Song, Y.; Zhu, B.; Zhu, S.; Zhu, J. A Scalable Fish-School Inspired Self-Assembled Particle System for Solar-Powered Water-Solute Separation. *Natl. Sci. Rev.* **2021**, *8*, No. nwab065.
(16) Peng, H.; Wang, D.; Fu, S. Unidirectionally Driving Nanofluidic Transportation via an Asymmetric Textile Pump for Simultaneous Salt-Resistant Solar Desalination and Drenching-Induced Power Generation. *ACS Appl. Mater. Interfaces* **2021**, *13*, 38405−38415.
(17) Huang, J.; He, Y.; Wang, L.; Huang, Y.; Jiang, B. Bifunctional Au@TiO2 Core−Shell Nanoparticle Films for Clean Water Generation by Photocatalysis and Solar Evaporation. *Energy Convers. Manag.* **2017**, *132*, 452−459.
(18) Lin, Y.; Xu, H.; Shan, X.; Di, Y.; Zhao, A.; Hu, Y.; Gan, Z. Solar Steam Generation Based on the Photothermal Effect: From Designs to Applications, and Beyond. *J. Mater. Chem. A* **2019**, *7*, 19203−19227.
(19) Fang, J.; Liu, J.; Gu, J.; Liu, Q.; Zhang, W.; Su, H.; Zhang, D. Hierarchical Porous Carbonized Lotus Seedpods for Highly Efficient Solar Steam Generation. *Chem. Mater.* **2018**, *30*, 6217−6221.
(20) Pham, T. T.; Nguyen, M. T.; Nguyen, H. G.; Nguyen, T. A. H.; Do, D. B.; Nguyen, D. C.; Tanaka, D.; Nguyen, D. D. Fe(III)-Natural Polyphenols Bilayer Coatings on Fingered Citron as a Novel Photothermal Material for Sustainable Seawater Desalination. *Desalination* **2022**, *537*, No. 115873.
(21) Guo, Q.; Yi, H.; Jia, F.; Song, S. Vertical Porous MoS2/Hectorite Double-Layered Aerogel as Superior Salt Resistant and Highly Efficient Solar Steam Generators. *Renewable Energy* **2022**, *194*, 68−79.
(22) Rastgar, M.; Jiang, L.; Wang, C.; Sadrzadeh, M. Aerogels in Passive Solar Thermal Desalination: A Review. *J. Mater. Chem. A* **2022**, *10*, 17857−17877.
(23) Li, W.; Li, X.; Chang, W.; Wu, J.; Liu, P.; Wang, J.; Yao, X.; Yu, Z. Z. Vertically Aligned Reduced Graphene Oxide/Ti3C2Tx MXene Hybrid Hydrogel for Highly Efficient Solar Steam Generation. *Nano Res.* **2020**, *13*, 3048−3056.
(24) Alam, Md. K.; He, M.; Chen, W.; Wang, L.; Li, X.; Qin, X. Stable and Salt-Resistant Janus Evaporator Based on Cellulose Composite Aerogels from Waste Cotton Fabric. *ACS Appl. Mater. Interfaces* **2022**, *14*, 41114−41121.
(25) Liu, H.; Alam, M. K.; He, M.; Liu, Y.; Wang, L.; Qin, X.; Yu, J. Sustainable Cellulose Aerogel from Waste Cotton Fabric for High-Performance Solar Steam Generation. *ACS Appl. Mater. Interfaces* **2021**, *13*, 49860−49867.
(26) Do, N. H. N.; Tran, V. T.; Tran, Q. B. M.; Le, K. A.; Thai, Q. B.; Nguyen, P. T. T.; Duong, H. M.; Le, P. K. Recycling of Pineapple Leaf and Cotton Waste Fibers into Heat-Insulating and Flexible Cellulose Aerogel Composites. *J. Polym. Environ.* **2021**, *29*, 1112−1121.
(27) Li, W.; Jian, H.; Wang, W.; Yu, D. Highly Efficient Solar Vapour Generation via Self-Floating Three-Dimensional Ti2O3-Based Aerogels. *Colloids Surf., A* **2022**, *634*, No. 128031.
(28) Wu, Z.; Sun, H.; Xu, Z.; Chi, H.; Li, X.; Wang, S.; Zhang, T.; Zhao, Y. Underwater Mechanically Tough, Elastic, Superhydrophilic Cellulose Nanofiber-Based Aerogels for Water-in-Oil Emulsion Separation and Solar Steam Generation. *ACS Appl. Nano Mater.* **2021**, *4*, 8979−8989.
(29) Wen, B.; Zhang, X.; Yan, Y.; Huang, Y.; Lin, S.; Zhu, Y.; Wang, Z.; Zhou, B.; Yang, S.; Liu, J. Tailoring Polypyrrole-Based Janus Aerogel for Efficient and Stable Solar Steam Generation. *Desalination* **2021**, *516*, No. 115228.
(30) Chu, A.; Yang, M.; Yang, H.; Shi, X.; Chen, J.; Fang, J.; Wang, Z.; Li, H. Sustainable Self-Cleaning Evaporators for Highly Efficient Solar Desalination Using a Highly Elastic Sponge-like Hydrogel. *ACS Appl. Mater. Interfaces* **2022**, *14*, 36116−36131.
(31) Yang, T.; Mu, X.; Zhou, J.; Wang, P.; Chen, H.; Wang, X.; Miao, L. A Robust Agar−PAM Hydrogel for Efficient Solar Steam Generation. *Solar RRL* **2022**, *6*, No. 2200586.
(32) Jiang, Q.; Tian, L.; Liu, K-K.; Tadepalli, S.; Raliya, R.; Biswas, P.; Naik, R. R.; Singamaneni, S. Bilayered Biofoam for Highly Efficient Solar Steam Generation. *Adv. Mater.* **2016**, *28*, 9400−9407.
(33) Tan, M.; Wang, J.; Song, W.; Fang, J.; Zhang, X. Self-Floating Hybrid Hydrogels Assembled with Conducting Polymer Hollow Spheres and Silica Aerogel Microparticles for Solar Steam Generation. *J. Mater. Chem. A* **2019**, *7*, 1244−1251.
(34) Mu, P.; Zhang, Z.; Bai, W.; He, J.; Sun, H.; Zhu, Z.; Liang, W.; Li, A. Superwetting Monolithic Hollow-Carbon-Nanotubes Aerogels with Hierarchically Nanoporous Structure for Efficient Solar Steam Generation. *Adv. Energy Mater.* **2019**, *9*, No. 1802158.
(35) Yang, E.; Wei, N.; Li, M.; Xu, R.; Sui, Y.; Kong, M.; Ran, X.; Cui, H. Three-Dimensional Artificial Transpiration Structure Based on 1T/2H-MoS2/Activated Carbon Fiber Cloth for Solar Steam Generation. *ACS Appl. Mater. Interfaces* **2022**, *14*, 29788−29796.
(36) Zou, Y.; Zhao, J.; Zhu, J.; Guo, X.; Chen, P.; Duan, G.; Liu, X.; Li, Y. A Mussel-Inspired Polydopamine-Filled Cellulose Aerogel for Solar-Enabled Water Remediation. *ACS Appl. Mater. Interfaces* **2021**, *13*, 7617−7624.
(37) Shao, Y.; Tang, J.; Li, N.; Sun, T.; Yang, L.; Chen, D.; Zhi, H.; Wang, D.; Liu, H.; Xue, G. Designing a bioinspired synthetic tree by unidirectional freezing for simultaneous solar steam generation and salt collection. *EcoMat* **2020**, *2*, No. e12018.
(38) Lim, H.; Kim, M.; Yoo, J.; Lee, D.; Lee, M.; Na, B.; Kim, S. K. Environmentally safe and renewable solar vapor generation device based on Prussian blue nanoparticles immobilized on cellulose nanofibers. *Desalination* **2022**, *524*, No. 115477.
(39) Tian, Y.; Liu, X.; Xu, S.; Li, J.; Caratenuto, A.; Mu, Y.; Wang, Z.; Chen, F.; Yang, R.; Liu, J.; Minus, M. L.; Zheng, Y. Recyclable and efficient ocean biomass-derived hydrogel photothermal evaporator for thermally-localized solar desalination. *Desalination* **2022**, *523*, No. 115449.
(40) Lin, X.; Wang, P.; Hong, R.; Zhu, X.; Liu, Y.; Pan, X.; Qiu, X.; Qin, Y. Fully Lignocellulosic Biomass-Based Double-Layered Porous Hydrogel for Efficient Solar Steam Generation. *Adv. Funct. Mater.* **2022**, *32*, No. 2209262.
(41) Pham, T. T.; Nguyen, T. H.; Nguyen, T. A. H.; Pham, D. D.; Nguyen, D. C.; Do, D. B.; Nguyen, H. V.; Ha, M. H.; Nguyen, Z. H. Durable, Scalable and Affordable Iron (III) Based Coconut Husk Photothermal Material for Highly Efficient Solar Steam Generation. *Desalination* **2021**, *518*, No. 115280.
(42) Do, N. H. N.; Luu, T. P.; Thai, Q. B.; Le, D. K.; Chau, N. D. Q.; Nguyen, S. T.; Le, P. K.; Phan-Thien, N.; Duong, H. M. Advanced Fabrication and Application of Pineapple Aerogels from Agricultural Waste. *Mater. Technol.* **2020**, *35*, 807−814.
(43) Nguyen, T. T. V.; Tri, N.; Tran, B. A.; Dao, D. T.; Nguyen, S. T.; Nguyen, T. A.; Phan, A. N.; Mai, T. P.; Huynh, H. K. P. Synthesis, Characteristics, Oil Adsorption, and Thermal Insulation Performance of Cellulosic Aerogel Derived from Water Hyacinth. *ACS Omega* **2021**, *6*, 26130−26139.

https://doi.org/10.1021/acs.langmuir.3c00297
Langmuir 2023, 39, 6780−6793

(44) Do, N. H. N.; Tran, V. T.; Tran, Q. B. M.; Le, K. A.; Thai, Q. B.; Nguyen, P. T. T.; Duong, H. M.; Le, P. K. Recycling of Pineapple Leaf and Cotton Waste Fibers into Heat-Insulating and Flexible Cellulose Aerogel Composites. *J. Polym. Environ.* **2021**, *29*, 1112−1121.
(45) Loh, J. W.; Goh, X. Y.; Nguyen, P. T. T.; Thai, Q. B.; Ong, Z. Y.; Duong, H. M. Advanced Aerogels from Wool Waste Fibers for Oil Spill Cleaning Applications. *J. Polym. Environ.* **2022**, *30*, 681−694.
(46) Poletto, M.; Ornaghi Júnior, H. L.; Zattera, A. J. Native Cellulose: Structure, Characterization and Thermal Properties. *Materials* **2014**, *7*, 6105−6119.
(47) Gupta, S.; Pramanik, A. K.; Kailath, A.; Mishra, T.; Guha, A.; Nayar, S.; Sinha, A. Composition Dependent Structural Modulations in Transparent Poly(Vinyl Alcohol) Hydrogels. *Colloids Surf., B* **2009**, *74*, 186−190.
(48) Ni, A.; Lin, P.; Wang, X.; Fu, D.; Hua, S.; Pei, D.; Li, S.; Han, X.; Xia, Y.; Zhang, T. Facile Preparation of High Strength Aerogel Evaporator for Efficient Solar-Driven Water Purification. *Sustainable Mater. Technol.* **2022**, *32*, No. e00443.
(49) Chen, G.; Jiang, Z.; Li, A.; Chen, X.; Ma, Z.; Song, H. Cu-Based MOF-Derived Porous Carbon with Highly Efficient Photothermal Conversion Performance for Solar Steam Evaporation. *J. Mater. Chem. A* **2021**, *9*, 16805−16813.
(50) World Health Organization. *Safe Drinking-water from Desalination*; WHO Press: Geneva, 2011.

https://doi.org/10.1021/acs.langmuir.3c00297
Langmuir 2023, 39, 6780−6793